



Adduct-based p-doping of organic semiconductors

Nobuya Sakai¹, Ross Warren¹, Fengyu Zhang², Simantini Nayak^{3,4}, Junliang Liu⁵, Sameer V. Kesava¹, Yen-Hung Lin¹, Himansu S. Biswal⁶, Xin Lin², Chris Grovenor⁵, Tadas Malinauskas⁷, Aniruddha Basu⁸, Thomas D. Anthopoulos⁸, Vytautas Getautis⁷, Antoine Kahn², Moritz Riede¹, Pabitra K. Nayak^{1,9}✉ and Henry J. Snaith¹✉

Electronic doping of organic semiconductors is essential for their usage in highly efficient optoelectronic devices. Although molecular and metal complex-based dopants have already enabled significant progress of devices based on organic semiconductors, there remains a need for clean, efficient and low-cost dopants if a widespread transition towards larger-area organic electronic devices is to occur. Here we report dimethyl sulfoxide adducts as p-dopants that fulfil these conditions for a range of organic semiconductors. These adduct-based dopants are compatible with both solution and vapour-phase processing. We explore the doping mechanism and use the knowledge we gain to ‘decouple’ the dopants from the choice of counterion. We demonstrate that asymmetric p-doping is possible using solution processing routes, and demonstrate its use in metal halide perovskite solar cells, organic thin-film transistors and organic light-emitting diodes, which showcases the versatility of this doping approach.

Organic semiconductors are used in a wide range of cutting-edge technologies, such as light-emitting diodes, field-effect transistors and photovoltaic (PV) devices due to their structural and functional tunability^{1–5}. Organic semiconductors usually have low charge carrier mobilities and low intrinsic conductivity, as compared with those of their inorganic counterparts. This, therefore, often necessitates doping to increase the number of charge carriers, which leads to both filling traps and an improvement in charge conductivity for device applications^{6–9}. A wide range of molecular dopants have been used for p-type and n-type doping of organic semiconductors^{10–14}. However, challenges such as a poor doping efficiency^{15,16} and doping instability¹⁷ still exist. Complex chemical structures of dopants require expensive synthesis and purification steps. Dopant molecules become the counterions during the doping process and remain in the host organic semiconductor¹⁴. As the dopants and counterions are coupled, it is difficult to optimize their role separately. A further challenge is to achieve graded (asymmetric) doping in a device stack, or selective doping on one side of a charge conducting layer, especially using a solution-processing route¹⁸, which is needed for better performances of the devices. For this class of dopants, there is clearly the need for reliable and inexpensive dopants that circumvent the issues mentioned above.

Solutions of dimethyl sulfoxide (DMSO) with hydrobromic acid (HBr) have been used in the past for the oxidation of organic molecules during material synthesis, such as diphenylethane to benzyl, and acetophenones to arylglyoxals^{19–21}. They have also been used to alter the oxidation state of Pd²⁺ to Pd⁴⁺ in the synthesis of the inorganic compound Cs₂PdBr₆ (ref. ²²).

Here we report that DMSO–HBr adducts can act as effective and clean p-dopants for a wide range of organic semiconductors. Our approach is an in situ formation of the dopant from commercially available low-cost chemicals, without any complex synthetic routes. The doping process is clean as the by-products and unreacted doping agents leave the thin film. We further show that it is possible to select the counterion independently, unlike the case for previously reported p-dopants. We also present a solution-processible route to achieve asymmetric doping in organic semiconductor films, and demonstrate applications of the adduct-based doping process in metal halide perovskite-based solar cells, organic thin-film transistors (OTFTs) and organic light-emitting diodes (OLEDs).

We start by testing the ability of our proposed agents to dope a variety of organic semiconductors, which are used as hole-transporting material (HTM), in solution. In Fig. 1a and Supplementary Table 1, we show the chemical structure and ionization potentials, respectively, of the selected HTMs. We introduce to the HTM solution a mixture of DMSO and HBr in an ~1:2 molar ratio, which we denote as the adduct-forming agent (Methods). Figure 1b shows the absorbance spectra and photographs of the HTM solutions before and after the addition of the adduct-forming agent. We observe absorption features that correspond to oxidized organic molecules after the addition of the adduct-forming agent into all the HTM solutions. We choose 2,2',7,7'-tetrakis(*N,N*-di(4-methoxyphenyl)amino)-9,9'-spirobifluorene (spiro-OMeTAD) as the test bed. After the addition of the adduct-forming agent, we observe an absorption peak related to the monocation radical, spiro-OMeTAD^{•+}, at ~520 nm (Fig. 1b and Supplementary Fig. 1a)^{23,24}. We estimate

¹Clarendon Laboratory, Department of Physics, University of Oxford, Oxford, UK. ²Department of Electrical and Computer Engineering, Princeton University, Princeton, NJ, USA. ³Department of Chemistry, University of Oxford, Inorganic Chemistry Laboratory, Oxford, UK. ⁴Materials Chemistry Department, CSIR-Institute of Mineral and Materials Technology, Bhubaneswar, India. ⁵Department of Materials, University of Oxford, Oxford, UK. ⁶School of Chemical Sciences, National Institute of Science Education and Research, Bhubaneswar, India. ⁷Department of Organic Chemistry, Kaunas University of Technology, Kaunas, Lithuania. ⁸KAUST Solar Center (KSC), King Abdullah University of Science and Technology (KAUST), Thuwal, Kingdom of Saudi Arabia. ⁹TIFR Centre for Interdisciplinary Sciences, Tata Institute of Fundamental Research, Hyderabad, India. ✉e-mail: pabitra.nayak@tifrr.res.in; henry.snaith@physics.ox.ac.uk

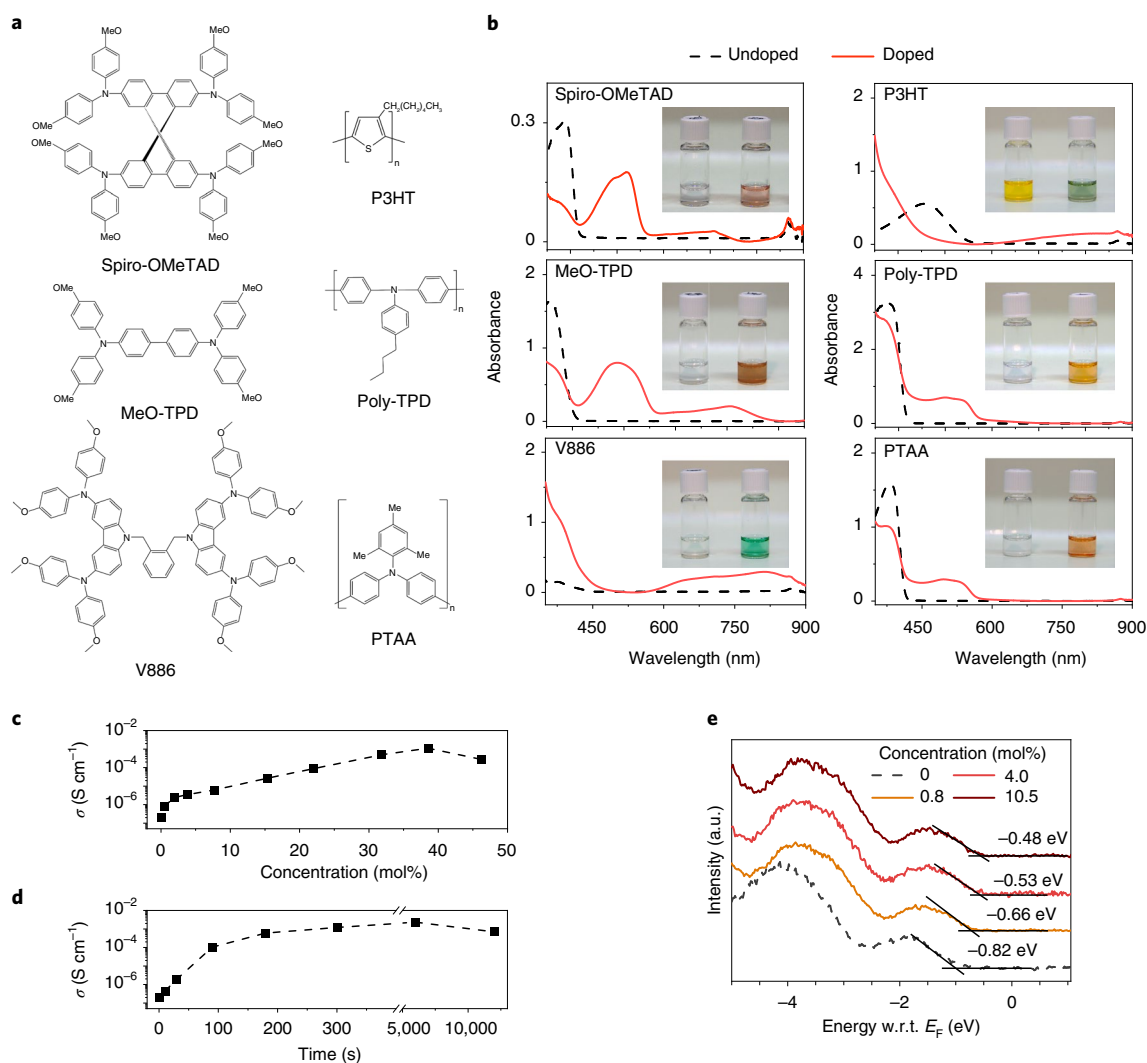


Fig. 1 | Doping ability of the DMSO-HBr adduct for various HTMs. **a**, Chemical structures of the HTMs spiro-OMeTAD, MeO-TPD, 1,2-bis(3,6-(4,4'-dimethoxydiphenylamino)-9H-carbazol-9-methyl)benzene (V886), poly(3-hexylthiophene-2,5-diyl) (P3HT), poly-TPD and PTAA. **b**, Ultraviolet-visible absorption spectra of organic HTMs in chlorobenzene (1.9×10^{-6} M) before (dashed line) and after (continuous line) the addition of the adduct-forming agent. Insets: photographs of vials that contain the neat HTM solution (left) and HTM solution with the adduct-forming agent (right). **c,d**, Conductivity of the spiro-OMeTAD thin-film doped with DMSO-HBr by either adding the dopant directly to the HTM solution (**c**, solution process) or exposing the thin films to the DMSO-HBr vapour (**d**, vapour-phase process). **e**, UPS spectra of the undoped and doped (solution process) spiro-OMeTAD thin-films. a.u., arbitrary units; E_F , Fermi energy; w.r.t., with respect to.

the doping efficacy, defined by the molar ratio of the oxidized spiro-OMeTAD to the added DMSO, to be $\sim 17.5\%$ (Supplementary Fig. 1b). To explore the possibility of doping the HTM using vapour-phase techniques, we expose spiro-OMeTAD thin films to vapours of DMSO and HBr (Supplementary Fig. 2). As we show in Supplementary Fig. 3, there is a continuous increase in the absorbance, which corresponds to the oxidized species in the spiro-OMeTAD thin film with increasing vapour exposure time. This indicates that our doping strategy is compatible with both solution and vapour-phase processing.

From the current-voltage (I - V) curves of thin-film electrode-gap in-plane devices with and without doping (Supplementary Fig. 4), we estimate the conductivity of the HTM films. We find a 2–3 orders of magnitude increase in the conductivity for all the HTMs with ionization energy ≤ 5.2 eV after doping (Supplementary Table 1). In Supplementary Fig. 5 we show I - V characteristics for the material with the deepest highest-occupied molecular orbital (HOMO) we found that we could dope, with an ionization energy of ~ 5.5 eV.

We also evaluate the conductivity of the doped spiro-OMeTAD films using a four-probe method²⁵, which reach a maximum conductivity of $\sim 2 \times 10^{-3} \text{ S cm}^{-1}$ (Fig. 1c,d) for both the solution and vapour-phase doping processes. This is higher than those achieved for this HTM with other dopants^{26–29} (Supplementary Fig. 6). To gain further insight into the doping effect, we perform ultraviolet photoelectron spectroscopy (UPS), X-ray photoelectron spectroscopy (XPS) and Kelvin-probe based contact potential difference measurements on the HTM thin films. We show the UPS spectra of the undoped and doped films of spiro-OMeTAD in Fig. 1e and the work function values measured by the Kelvin-probe method in Supplementary Fig. 7. As expected for p-type doping, the work function of the doped film increases and the Fermi level shifts closer to the HOMO level of the HTM. In Supplementary Fig. 8, we show the XPS spectra of the doped films. We observe that the C 1s, O 1s and N 1s peaks shifting to lower binding energies with an increase in the concentration of the adduct-forming agent, which provides further confirmation of p-doping³⁰. In Supplementary

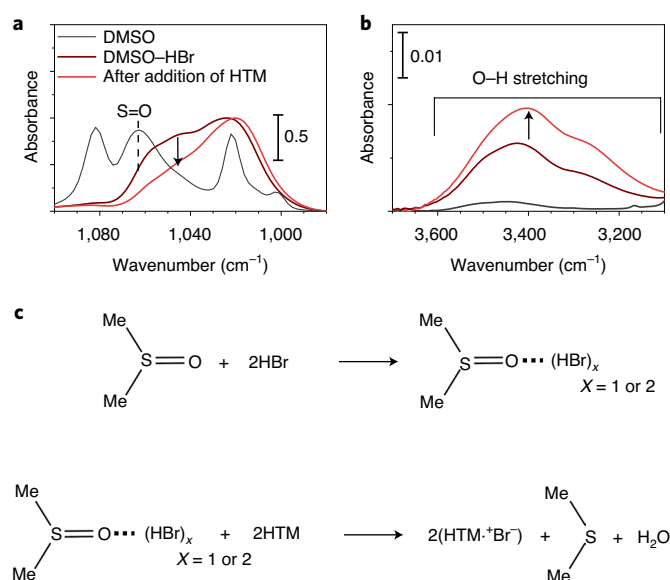


Fig. 2 | Mechanism of doping by the DMSO-HBr adduct. a, b, FTIR spectra of the DMSO-HBr mixture in chlorobenzene and after the addition of spiro-OMeTAD showing the consumption of the adduct and formation of H₂O during the doping process in the region of S=O absorbance (**a**) and that of OH stretching absorbance (**b**). **c,** Proposed mechanism of the doping process.

Fig. 9, we report similar UPS and XPS shifts on doping for another HTM, *N,N,N',N'*-tetrakis(4-methoxyphenyl)benzidine (MeO-TPD).

That neither DMSO nor HBr can dope the HTMs alone indicates that it is essential for both compounds to come together for the doping process to happen (Supplementary Fig. 10). We investigate the doping mechanism by in situ attenuated total reflection Fourier transform infrared spectroscopy (FTIR) and gas chromatographic mass spectrometry. In the FTIR spectrum of a DMSO solution in chlorobenzene (Fig. 2a), we observe that the peak around ~1,060 cm⁻¹, which corresponds to the absorbance of the S=O bond³¹ of DMSO, broadens and shifts to a lower wavenumber (around 1,020–1,050 cm⁻¹) after the addition of HBr, which indicates the lowering of the S=O bond strength^{22,31}. Based on quantum chemical calculations, we assign the peaks around ~1,035–1,055 cm⁻¹ to the formation of a molecular adduct between DMSO and HBr (Supplementary Fig. 11). We then add the spiro-OMeTAD solution to the adduct solution and record the change in the absorbance spectra over time. We observe a continuous decrease in the peak intensity at ~1,050 cm⁻¹, which indicates the consumption of the DMSO-HBr adduct and breaking of the sulfur-oxygen bond (Supplementary Fig. 12). Concurrently, we also recorded an increase in the absorbance of OH stretching around ~3,400 cm⁻¹ (Fig. 2b)³², which indicates that H₂O is one of the by-products of the process. From gas chromatographic mass spectrometry of the released gases during the doping process, we identify dimethyl sulfide as another by-product (Supplementary Fig. 13). Based on this information, we propose the following mechanism for the doping. As the DMSO-HBr adduct accepts electron(s) from the HOMO level of the organic molecule, the activated DMSO reduces to dimethyl sulfide, one of the by-products. The oxidation states of sulfur in DMSO and dimethyl sulfide are 0 and -2, respectively. The positive charge on the host organic cation is counterbalanced by the bromide anion from HBr. The oxygen from DMSO and H from the HBr molecule then form H₂O, as another by-product. We show the probable mechanism schematically in Fig. 2c. Apart from the Br⁻ counterion, which must be retained in the film to retain charge

neutrality, we highlight that the doping process does not leave behind the by-products or unreacted dopants in the organic semiconductor matrix, which we confirm by the FTIR and XPS measurements on doped spiro-OMeTAD films (Supplementary Note 1 and Supplementary Figs. 14 and 15). However, similar systems, such as DMSO-HCl and DMSO-HI adducts, are not suitable for p-type doping owing to their low efficiency and instability, respectively (Supplementary Note 2 and Supplementary Figs. 16–18).

Although the DMSO-HBr doping is clean and efficient, a critical factor for the utility of a doping process is that it must be stable under the conditions experienced during the manufacturing of additional layers in the device stack, particularly at elevated temperatures. We use conductivity and ellipsometry-based optical measurements to investigate the thermal stability of the doped films. To assess if the counterion diffuses between layers, we constructed devices with a double layer of doped and undoped HTMs, which comprised a bottom-contact gold electrode on a Si substrate (Fig. 3a), a spin-coated doped layer of MeO-TPD, followed by a thermally evaporated layer of intrinsic MeO-TPD.

If dedoping or migration of the doped organic molecule/counterion occurs due to thermal stress, we expect the conductivity and ellipsometric profiles of the films to change.¹⁷ As we show in Fig. 3b and Supplementary Fig. 19a, we do not observe any change in the conductivity of the sample, nor any change in the ellipsometric profile (phase difference Δ and amplitude ratio Ψ) over a period of 100 hours at 50 °C. The simulated profiles (Supplementary Note 3 and Supplementary Fig. 19b) for the doped and non-doped mixed films are different to the observed profiles, which confirms that the migration of the doped material (or counterion) does not happen during the stress test at 50 °C for 100 hours.

To further study the impact of doping on the morphology of the organic films, which is highly relevant for device applications, we perform atomic force microscopy (AFM) measurements of MeO-TPD films with different doping concentrations and after different levels of thermal stressing. We observe no considerable changes in the topography (Fig. 3d and Supplementary Fig. 20) for the doped films as compared with that of the undoped films, both before and after thermal stressing.

Despite being stable at 50 °C, as we show in Fig. 3c, when we raise the temperature to 85 °C we observe a decrease in the conductivity in films doped with the DMSO-HBr adduct, which indicates dedoping, presumably owing to the diffusion of Br⁻ and subsequent escape from the matrix as Br₂. HBr plays a dual role in the doping process—as an activator and then as a provider of the anion. Our doping mechanism should allow us to introduce other anions, specifically chosen for an improved thermal stability of the doped material or for other properties, which would therefore be decoupled from the dopant. To demonstrate that such ‘decoupling’ of the dopant and counterion is feasible, we chose a combination of 10-camphorsulfonic acid (CSA), DMSO and HBr. We estimate via a van der Waals surface calculation that the counterion, camphorsulfonate, is ~8.5 times bulkier than the bromide³³. The larger size of camphorsulfonate could probably reduce the diffusivity and volatility issues associated with bromide. In Supplementary Figs. 21–24, we show the doping ability of the DMSO-HBr-CSA system in spiro-OMeTAD and MeO-TPD by absorbance, conductivity, UPS and XPS studies. No doping occurs in the spiro-OMeTAD solution when we add DMSO-CSA only, unlike DMSO-HBr (Supplementary Fig. 25). However, we only need to add a small volume (~9 mol% with respect to CSA) of aqueous HBr to ‘activate’ the doping process. We determine that the doping efficiency of the DMSO-HBr-CSA system is ~22% (with respect to the added CSA molecules) for spiro-OMeTAD from the optical absorbance change (Supplementary Fig. 21). For the films doped with DMSO-HBr-CSA, we observe no noticeable change in the conductivity

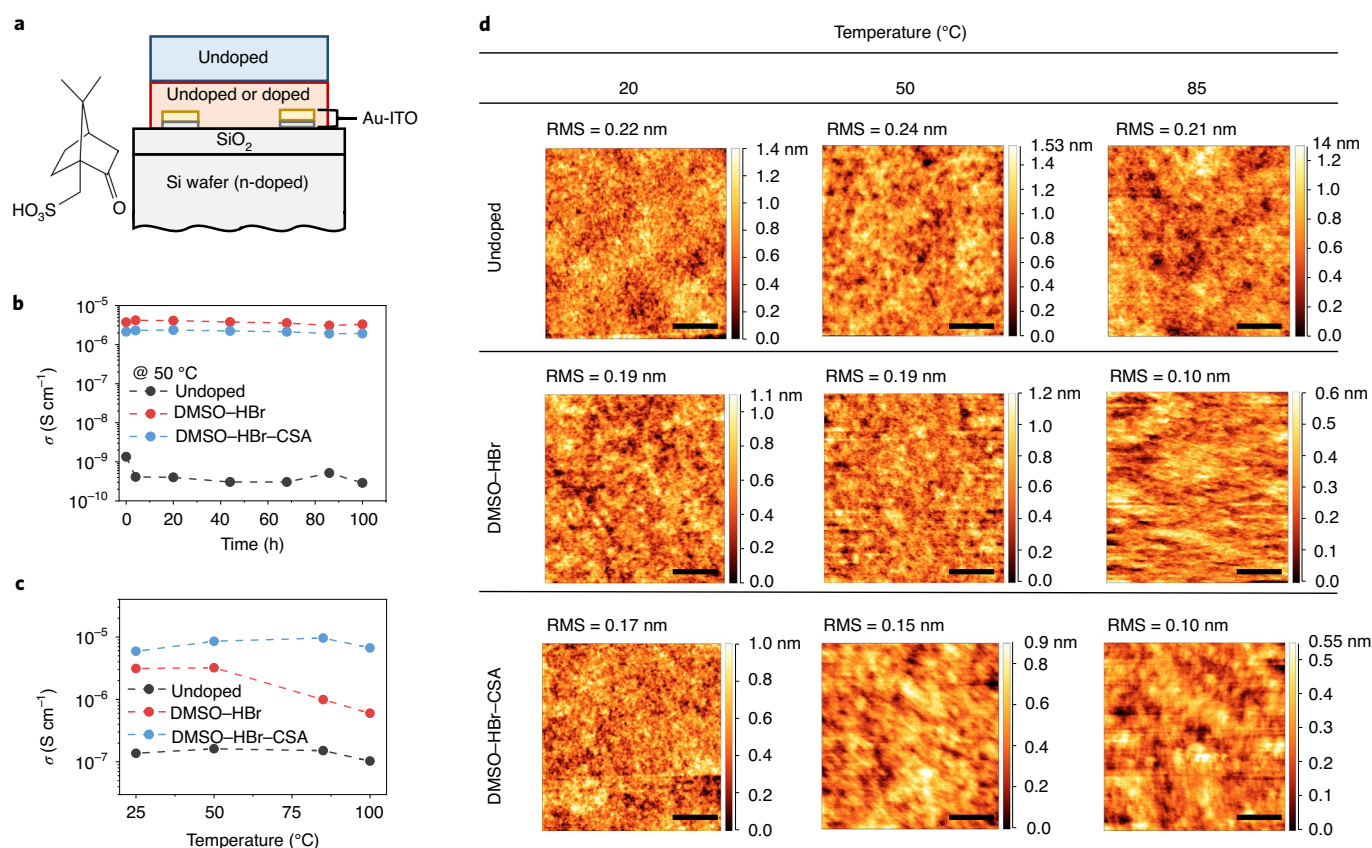


Fig. 3 | Thermal stability of the doped MeO-TPD films. **a**, Chemical structure of CSA (left) and a schematic illustration of the geometry to evaluate the thermal stability of dopants by conductivity measurements (right). **b**, Conductivity of the MeO-TPD films doped with DMSO-HBr and DMSO-HBr-CSA after thermal stressing at 50 °C for 100 h. **c**, Conductivity (at room temperature) of undoped and doped MeO-TPD films with DMSO-HBr and DMSO-HBr-CSA after stressing at different temperatures for 10 min on a hotplate in a nitrogen-filled glove box. **d**, AFM topography images of the undoped and doped MeO-TPD films. The AFM images are taken after the films are incubated at 20 °C (left column), 50 °C (middle column) and 85 °C for 10 min. Scale bars, 500 nm. Root mean square (r.m.s.) height variation is evaluated over $2 \times 2 \mu\text{m}^2$ for each AFM image.

(Figs. 3b,c) and morphology (Fig. 3d and Supplementary Fig. 26) with prolonged thermal stressing, even at 100 °C. We present here only one example for the counterion exchange but, in principle, many other counterions tailored to specific needs could also be used (see Supplementary Notes 4 and 5 and Supplementary Fig. 27 for the mechanism of doping by the DMSO-HBr-CSA system and its further applications).

One of the primary means to minimize contact resistance and create diode-like behaviour in semiconductor devices is to employ asymmetric doping, with the highly doped region in contact with the electrode material^{18,34–37}. A key breakthrough for OLEDs has been the controlled p- and n-type doping of organic charge transport materials combined with the deposition of multiple layers of different organic semiconductors on one another³⁸. For OLEDs, this is usually done via thermal evaporation of the organic semiconductors in vacuum^{39,40}.

For solution-based processes, it is challenging to coat two subsequent layers on top of each other due to the common solubility of the host and dopants. We explore the possibility of asymmetric doping (that is, the doping is predominantly at one interface) via our adduct methods. To that end, we prepare a ‘hole-only’ device with a stack of FTO/poly-TPD(350 nm)/Au (FTO, fluorine-doped tin oxide; poly-TPD, poly(*N,N'*-bis(4-butylphenyl)-*N,N'*-bisphenylbenzidine)) and introduce a CSA–DMSO–HBr layer (via a solution process) either at the interface between poly-TPD and Au or at the interface between poly-TPD and FTO.

In Fig. 4a–c, we show the current density–voltage (*J*–*V*) curves of the hole-only devices in which the interface and bulk are doped differently for each device. In Fig. 4a, the current density in the positive bias (that is, hole injection from the Au electrode) is clearly higher for the device with a doped poly-TPD:Au interface when compared with that of the undoped device. For the doped device, the current density increases with the dopant concentration in the doped layer, which we controlled via the concentration of the CSA (Supplementary Fig. 28a). Under a negative bias (that is, hole injection from the FTO side), the current densities are similar for both the asymmetrically doped and undoped devices. As would be expected for the case of interface doping, we observe the opposite trend in the *J*–*V* curves (Fig. 4b and Supplementary Fig. 28b) for the devices in which the doping is introduced at the FTO:poly-TPD interface with an increased current density for the interface-doped device under a negative bias. As we show in Fig. 4c, for homogeneous doping the increases in the current densities are similar for both negative and positive bias.

To explore the positional localization of the space charge regions of the hole-only devices with interface doping, we perform capacitance–voltage measurements (Supplementary Fig. 29) and use Mott–Schottky analysis to estimate the acceptor density (N_A) as a function of the depletion width from the conductive electrode–organic semiconductor junction (Supplementary Note 6)^{41–43}. When we profile the N_A in the proximity of the doped interfaces, we find that the N_A values in the devices for the doped poly-TPD:Au

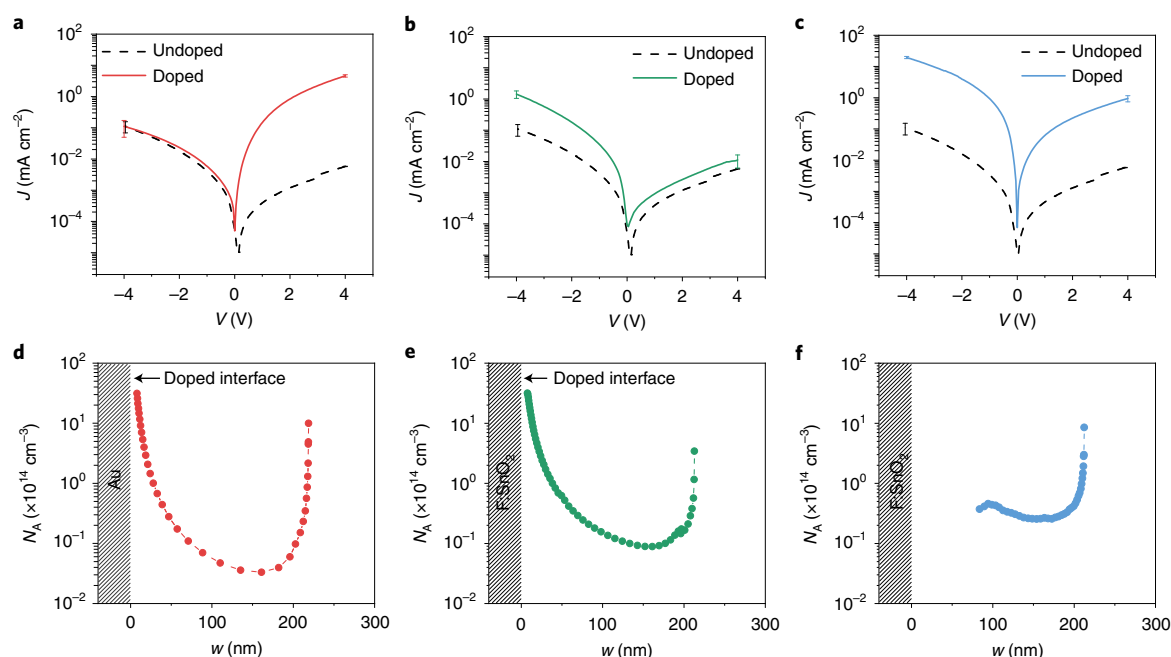


Fig. 4 | Asymmetric doping in hole-only devices. a–c, J - V curves of the hole-only devices doped at the poly-TPD:Au interface (**a**), at the FTO:poly-TPD interface (**b**) and with homogeneous doping (**c**). **d–f,** N_A as a function of the depletion width (w) of hole-only devices doped at the poly-TPD:Au interface (**d**), at the FTO:poly-TPD interface (**e**) and with homogeneous doping (**f**).

interface (Fig. 4d) and doped FTO:poly-TPD interface (Fig. 4e) exhibit a gradient profile. The N_A follows a gradual decrease when the depletion width progresses further away from these doped interfaces, followed by a steep increase when the calculated depletion width approaches the width of the complete diode. In Fig. 4f, we show the N_A profile of the homogeneously doped devices. Compared with the undoped device (Supplementary Fig. 30), we see a higher N_A value for the homogeneously doped device.

To further investigate the asymmetric doping, we perform secondary ion mass spectrometry measurements of the doped and undoped films. We use silicon as a substrate. Because the HTM (MeO-TPD) does not contain sulfur, mapping of sulfur signal can be used to determine the distribution of the counter ions (CSA^-) in the doped film. In Supplementary Figs. 31 and 32, we show the depth profiles of sulfur in undoped as well as doped films. For the films that we intended to dope at the top surface, we observe a significant enhancement of the sulfur signal at this interface (Supplementary Note 7 and Supplementary Fig. 31b), and for the films doped at the buried HTM:Si interface, we observe sulfur enrichment at this buried interface (Supplementary Fig. 32). This enhancement of sulfur at the intended interfaces further confirms asymmetric doping.

We now demonstrate the utility of the doping methods in three types of optoelectronic devices that benefit from doped charge transport layers: OTFTs, perovskite solar cells (PSCs) and OLEDs (device architectures in Fig. 5a–c).

We fabricate indacenodithiophene–benzothiadiazole (C_{16} IDT-BT)-based OTFTs in a top-gate bottom-contact device architecture (Fig. 5a)⁴⁴. Figure 5d shows the transfer I - V characteristics measured from OTFTs fabricated using pristine and moderately and heavily doped C_{16} IDT-BT based on the solution-processed DMSO–HBr adduct doping approach (denoted as DMSO–HBr (M) and DMSO–HBr (H), respectively). We observe higher on-current levels and positively shifted turn-on voltages due to p-doping. In Supplementary Table 3 and Supplementary Fig. 33, we summarize the performance parameters from the transfer characteristics and provide a detailed analysis of the areal trap density (as compared with that of the undoped device) and the trap concentration per

unit energy⁴⁵ (Supplementary Note 8). We achieve a clear improvement in the field-effect mobility (Supplementary Table 3) by the adduct-based doping. We further confirm that DMSO–HBr–CSA adduct doping assists hole transport in OTFTs (Supplementary Fig. 34 and Supplementary Table 4).

For perovskite ($\text{FA}_{0.83}\text{Cs}_{0.17}\text{Pb}(\text{I}_{0.85}\text{Br}_{0.15})_3$ (FA, formamidinium)) solar cells, we use spiro-OMeTAD as the HTM with the doping methods presented here and compared them with other doping methods commonly used, such as doping with LiTFSI–oxygen or Co(III)TFSI (TFSI, bis-(tri-fluoromethylsulfonyl)imide) (Supplementary Fig. 35 and Supplementary Table 5). In Fig. 5e, we show the J - V curves and steady-state power output (SPO) of our best-performing solar cells, in which the HTM is doped with the DMSO–adduct-based dopant or LiTFSI–oxygen. We find that the devices in which the HTM is doped with DMSO–HBr or DMSO–HBr–CSA show a significantly improved power conversion efficiency (PCE) and SPO as compared with those of the commonly used doping methods (Fig. 5e). We summarize the PV performance parameters in Table 1. In the Supplementary Information, we show additional information to corroborate the PV properties with our new doping, such as cross-sectional scanning electron micrographs of devices, external quantum efficiencies and forward and reverse scan directions of the J - V curves (Supplementary Fig. 36–38 and Supplementary Table 6). We also demonstrate the doping capability of DMSO–HBr–CSA on poly(bis(4-phenyl)(2,4,6-trimethylphenyl)amine (PTAA) in n–i–p PSCs, without *tert*-butylpyridine and LiTFSI (Supplementary Fig. 39).

The Fermi level in the HTM monotonically shifts closer to the HOMO level onset with increasing dopant concentration (Fig. 1e). In the complete solar cell, the Fermi level alignment between the HTM and the quasi-Fermi level for holes in the perovskite absorber layer, and between the HTM and the Fermi level of the metallic electrode, are likely to improve with increased doping. Therefore, the increased V_{oc} of the solar cells suggests an improved energetic alignment across these interfaces due to doping. The improvement in fill factor is consistent with a reduced series resistance in the cell, which results from increased conductivity of the HTM. Therefore, both these effects, Fermi level deepening and increased conductivity,

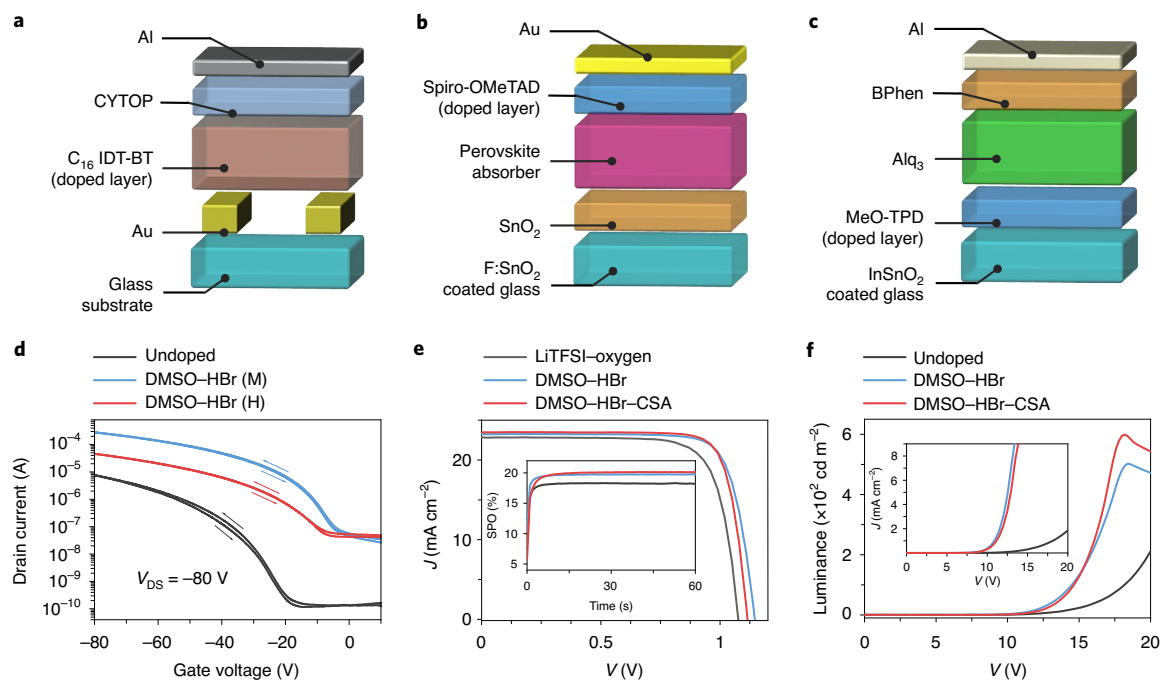


Fig. 5 | Usage of adduct-based dopants in optoelectronic devices. a–c, Schematics of the OTFT (**a**), the perovskite PV device (**b**) and the OLED (**c**). **d,** *I*–*V* characteristics of DMSO–HBr-doped C₁₆ IDT–BT-based OTFT. **e,** *J*–*V* curves of the solar cells with different dopants and counterions. Inset: SPO for the respective PSCs at a fixed maximum power point voltage. **f,** Luminescence–voltage curve for the OLEDs with different dopants and counterions. Inset: *J*–*V* curves of the OLEDs. Alq₃, tris-(8-hydroxyquinoline)aluminium; BPhen, bathophenanthroline; ITO, indium tin oxide; V_{DS}, drain-source voltage.

Table 1 | Performance parameters of PSCs doped with a DMSO-adduct-based dopant

Doping method	J_{sc} (mA cm ⁻²)	V_{oc} (V)	FF	PCE (%)	R_s (Ω)	SPO (%)
LiTFSI-oxygen	22.8	1.08	0.76	18.7	39.9	18.2
DMSO-HBr	23.2	1.14	0.79	21.1	38.9	19.8
DMSO-HBr-CSA	23.5	1.11	0.81	21.3	32.5	20.1

J_{sc} , short-circuit current density; V_{oc} , open-circuit voltage; FF, fill factor; R_s , series resistance.

appear to contribute to the improved performance in the solar cells (see Supplementary Note 9 and Supplementary Fig. 40 for discussion on the increased short-circuit current due to doping)

We fabricate OLEDs with the prototypical Alq₃ as the emitting material, sandwiched between MeO-TPD as the hole transport layer and BPhen as the electron transport layer (Fig. 5c). We show the luminescence–voltage curves in Fig. 5f and the *J*–*V* curves in the inset, and the electroluminescence spectrum in Supplementary Fig. 41. We observe an increase in current density and luminance for OLEDs when the MeO-TPD layer is doped with DMSO–HBr or DMSO–HBr–CSA, in comparison with those of the undoped device. We attribute the improvement in the luminance to the improved charge injection with the doped HTMs. We also evaluate the performance of the OLED doped with F4TCNQ (2,3,5,6-tetrafluoro-7,7,8,8-tetracyanoquinodimethane) as a typical p-dopant (Supplementary Fig. 42). We find that the OLEDs prepared with the widely used p-dopant F4TCNQ performance is comparable with that of our DMSO-adduct-based dopant.

In conclusion, we have demonstrated a DMSO-adduct-based p-doping scheme, applicable to a variety of organic HTMs, which range from small molecules to polymers. From understanding the doping mechanism, we decouple the dopant from the counterions, which allow the electronic and physical properties and thermal stability of the doped HTM to be tuned separately. We also

demonstrate that asymmetric doping is possible, using an adduct-based doping method. We have shown the usage of the doped organic layers in OTFTs, PSCs and OLEDs. The p-doping method that we present here is not restricted to the DMSO–HBr adduct. In principle, it can be extended to other adduct systems in which different sulfoxide-containing molecules in combination with different activators should be feasible, which highlights an unexplored avenue to pursue for controlled doping of organic semiconductors.

Online content

Any methods, additional references, Nature Research reporting summaries, source data, extended data, supplementary information, acknowledgements, peer review information; details of author contributions and competing interests; and statements of data and code availability are available at <https://doi.org/10.1038/s41563-021-00980-x>.

Received: 12 June 2019; Accepted: 9 March 2021;

Published online: 22 April 2021

References

- Granström, M. et al. Laminated fabrication of polymeric photovoltaic diodes. *Nature* **395**, 257–260 (1998).
- Halls, J. J. M. et al. Efficient photodiodes from interpenetrating polymer networks. *Nature* **376**, 498–500 (1995).

3. Sirringhaus, H. et al. Two-dimensional charge transport in self-organized, high-mobility conjugated polymers. *Nature* **401**, 685–688 (1999).
4. Tang, C. W. & Vanslyke, S. A. Organic electroluminescent diodes. *Appl. Phys. Lett.* **51**, 913–915 (1987).
5. Yu, G., Gao, J., Hummelen, J. C., Wudl, F. & Heeger, A. J. Polymer photovoltaic cells: enhanced efficiencies via a network of internal donor–acceptor heterojunctions. *Science* **270**, 1789–1791 (1995).
6. Blochwitz, J., Pfeiffer, M., Fritz, T. & Leo, K. Low voltage organic light emitting diodes featuring doped phthalocyanine as hole transport material. *Appl. Phys. Lett.* **73**, 729–731 (1998).
7. Maennig, B. et al. Controlled p-type doping of polycrystalline and amorphous organic layers: self-consistent description of conductivity and field-effect mobility by a microscopic percolation model. *Phys. Rev. B* **64**, 195208 (2001).
8. Godet, C. Variable range hopping revisited: the case of an exponential distribution of localized states. *J. Non-Cryst. Solids* **302**, 333–338 (2002).
9. Rubel, O., Baranovskii, S. D., Thomas, P. & Yamasaki, S. Concentration dependence of the hopping mobility in disordered organic solids. *Phys. Stat. Sol.* **171**, 168–171 (2004).
10. Blochwitz, J. et al. Interface electronic structure of organic semiconductors with controlled doping levels. *Org. Electron.* **2**, 97–104 (2001).
11. Gao, W. & Kahn, A. Controlled p-doping of zinc phthalocyanine by coevaporation with tetrafluorotetracyanoquinodimethane: a direct and inverse photoemission study. *Appl. Phys. Lett.* **79**, 4040–4042 (2001).
12. Harada, K. et al. Organic homojunction diodes with a high built-in potential: interpretation of the current–voltage characteristics by a generalized Einstein relation. *Phys. Rev. Lett.* **94**, 36601 (2005).
13. Chan, C. K., Zhao, W., Barlow, S., Marder, S. & Kahn, A. Decamethylcobaltocene as an efficient n-dopant in organic electronic materials and devices. *Org. Electron.* **9**, 575–581 (2008).
14. Lin, X. et al. Beating the thermodynamic limit with photo-activation of n-doping in organic semiconductors. *Nat. Mater.* **16**, 1209–1215 (2017).
15. Tietze, M. L. et al. Elementary steps in electrical doping of organic semiconductors. *Nat. Commun.* **9**, 1182 (2018).
16. Tietze, M. L., Burtone, L., Riede, M., Lüssem, B. & Leo, K. Fermi level shift and doping efficiency in p-doped small molecule organic semiconductors: a photoelectron spectroscopy and theoretical study. *Phys. Rev. B* **035320**, 1–12 (2012).
17. Li, J. et al. Measurement of small molecular dopant F4TCNQ and C₆₀F₃₆ diffusion in organic bilayer architectures. *ACS Appl. Mater. Interfaces* **7**, 28420–28428 (2015).
18. Kolesov, V. A. et al. Solution-based electrical doping of semiconducting polymer films over a limited depth. *Nat. Mater.* **16**, 474–481 (2017).
19. Yusubov, M. S., Filimonov, V. D. & Ogorodnikov, V. D. Dimethyl sulfoxide–hydrobromic acid as a novel reagent for convenient oxidation on a preparative scale of stilbenes and some derivatives of diphenylethane to benzils. *Bull. Acad. Sci. USSR Div. Chem. Sci.* **40**, 766–770 (1991).
20. Lee, T. V. Oxidation adjacent to oxygen of alcohols by activated DMSO methods. *Compr. Org. Synth.* **7**, 291–303 (1991).
21. Floyd, M. B., Du, M. T., Fabio, P. F., Jacob, L. A. & Johnson, B. D. The oxidation of acetophenones to arylglyoxals with aqueous hydrobromic acid in dimethyl sulfoxide. *J. Org. Chem.* **50**, 5022–5027 (1985).
22. Sakai, N. et al. Solution-processed cesium hexabromopalladate(IV), Cs₂PdBr₆, for optoelectronic applications. *J. Am. Chem. Soc.* **139**, 6030–6033 (2017).
23. Cappel, U. B., Daeneke, T. & Bach, U. Oxygen-induced doping of spiro-MeOTAD in solid-state dye-sensitized solar cells and its impact on device performance. *Nano Lett.* **12**, 4925–4931 (2012).
24. Burschka, J. et al. Tris(2-(1H-pyrazol-1-yl)pyridine)cobalt(III) as p-type dopant for organic semiconductors and its application in highly efficient solid-state dye-sensitized solar cells. *J. Am. Chem. Soc.* **133**, 18042–18045 (2011).
25. Planells, M. et al. Diacetylene bridged triphenylamines as hole transport materials for solid state dye sensitized solar cells. *J. Mater. Chem. A* **1**, 6949–6960 (2013).
26. Abate, A. et al. Protic ionic liquids as p-dopant for organic hole transporting materials and their application in high efficiency hybrid solar cells. *J. Am. Chem. Soc.* **135**, 13538–13548 (2013).
27. Pellaroque, A. et al. Efficient and stable perovskite solar cells using molybdenum tris(dithiolene)s as p-dopants for spiro-OMeTAD. *ACS Energy Lett.* **2**, 2044–2050 (2017).
28. Nguyen, W. H., Bailie, C. D., Unger, E. L. & McGehee, M. D. Enhancing the hole-conductivity of spiro-OMeTAD without oxygen or lithium salts by using spiro(TFSI)₂ in perovskite and dye-sensitized solar cells. *J. Am. Chem. Soc.* **136**, 10996–11001 (2014).
29. Chen, C. et al. Cu(II) complexes as p-type dopants in efficient perovskite solar cells. *ACS Energy Lett.* **2**, 497–503 (2017).
30. Ono, L. K. et al. Air-exposure-induced gas-molecule incorporation into spiro-MeOTAD films. *J. Phys. Chem. Lett.* **5**, 1374–1379 (2014).
31. Fawcett, W. R. & Kloss, A. A. Solvent-induced frequency shifts in the infrared spectrum of dimethyl sulfoxide in organic solvents. *J. Phys. Chem.* **100**, 2019–2024 (1996).
32. Wallace, V. M., Dhumal, N. R., Zehentbauer, F. M., Kim, H. J. & Kiefer, J. Revisiting the aqueous solutions of dimethyl sulfoxide by spectroscopy in the mid- and near-infrared: experiments and Car–Parrinello simulations. *J. Phys. Chem. B* **119**, 14780–14789 (2015).
33. Zhao, Y. H., Abraham, M. H. & Zissimos, A. M. Fast calculation of van der Waals volume as a sum of atomic and bond contributions and its application to drug compounds. *J. Org. Chem.* **68**, 7368–7373 (2003).
34. Kang, K. et al. 2D coherent charge transport in highly ordered conducting polymers doped by solid state diffusion. *Nat. Mater.* **15**, 896–902 (2016).
35. Ávila, J. et al. High voltage vacuum-deposited CH₃NH₃PbI₃–CH₃NH₃PbI₃ tandem solar cells. *Energy Environ. Sci.* **11**, 3292–3297 (2018).
36. Abdi-Jalebi, M. et al. Charge extraction via graded doping of hole transport layers gives highly luminescent and stable metal halide perovskite devices. *Sci. Adv.* **5**, eaav2012 (2019).
37. Wanlass, M. Systems and methods for advanced ultra-high-performance InP solar cells. US patent 9590131B2 (2017).
38. Walzer, K., Maennig, B., Pfeiffer, M. & Leo, K. Highly efficient organic devices based on electrically doped transport layers. *Chem. Rev.* **107**, 1233–1271 (2007).
39. Pfeiffer, M., Beyer, A., Fritz, T. & Leo, K. Controlled doping of phthalocyanine layers by cosublimation with acceptor molecules: a systematic Seebeck and conductivity study. *Appl. Phys. Lett.* **73**, 3202–3204 (1998).
40. Nollau, A., Pfeiffer, M., Fritz, T. & Leo, K. Controlled n-type doping of a molecular organic semiconductor: naphthalenetetracarboxylic dianhydride (NTCDA) doped with bis(ethylenedithio)-tetrathiafulvalene (BEDT-TTF). *J. Appl. Phys.* **87**, 4340–4343 (2000).
41. Kirchartz, T. et al. Sensitivity of the Mott–Schottky analysis in organic solar cells. *J. Phys. Chem. C* **116**, 7672–7680 (2012).
42. Deledalle, F. et al. Understanding the effect of unintentional doping on transport optimization and analysis in efficient organic bulk-heterojunction solar cells. *Phys. Rev. X* **5**, 11032 (2015).
43. Zonno, I., Martinez-Otero, A., Hebig, J. & Kirchartz, T. Understanding Mott–Schottky measurements under illumination in organic bulk heterojunction solar cells. *Phys. Rev. Appl.* **7**, 034018 (2017).
44. Lin, Y.-H. et al. Deciphering photocarrier dynamics for tuneable high-performance perovskite–organic semiconductor heterojunction phototransistors. *Nat. Commun.* **10**, 4475 (2019).
45. Lin, Y.-H. et al. Hybrid organic–metal oxide multilayer channel transistors with high operational stability. *Nat. Electron.* **2**, 587–595 (2019).

Publisher's note Springer Nature remains neutral with regard to jurisdictional claims in published maps and institutional affiliations.

© The Author(s), under exclusive licence to Springer Nature Limited 2021

Methods

DMSO–HBr adduct doping. Preparation of DMSO–HBr adduct-forming agent. DMSO (150 ml, anhydrous, $\geq 99.9\%$; Aldrich) was added into 500 μl of aqueous HBr (48 wt%; Aldrich) and the solution was mixed by a vortex mixer for 1 min. The molar ratio of DMSO and HBr was $\sim 1:2$.

Doping of HTM in solution by the DMSO–HBr adduct. The adduct forming agent (1.5 μl) was added to 1 ml of the HTM solutions (small molecules $\sim 20\ \mu\text{M}$ and Polymers $\sim 25\ \mu\text{g ml}^{-1}$) in chlorobenzene or toluene and the solution was mixed by a vortex mixer. The solution was kept at room temperature for 20 min. The concentration of the adduct-forming agent in the HTM solutions was varied by adding different amounts of the adduct-forming agent.

Preparation of HTM thin films doped with the DMSO–HBr adduct in a solution process. The adduct-forming agent (10 μl) was added to 2.5 ml of 0.28 mM spiro-OMeTAD (luminescence technology) solution in chlorobenzene (anhydrous, $\geq 99.9\%$; Aldrich). The solution was mixed by a vortex mixer for 1 min and then kept for 20 min at room temperature to prepare a heavily doped spiro-OMeTAD solution. The heavily doped spiro-OMeTAD solution (3–15 μl) was added to 1 ml of undoped spiro-OMeTAD solution (70 mM) in chlorobenzene and the solution was kept for at least 15 min before thin film preparation. The resulting solution was spin coated onto the substrate at 2,500 r.p.m. for 45 s (acceleration, 500 r.p.m.) to prepare the thin film. A typical example for the preparation of doped thin film spiro-OMeTAD is provided here. Similar protocols were adapted for other HTMs: the concentration of the adduct-forming agent in the HTM solution was varied by changing the amount of adduct-forming agent in the HTM solution.

Preparation of HTM thin films doped with the DMSO–HBr adduct in a vapour phase process. A spiro-OMeTAD solution in chlorobenzene (70 mM) was spin coated onto the substrate at 2,500 r.p.m. for 45 s (acceleration, 500 r.p.m.). DMSO (1.5 μl) and aqueous HBr (5 μl) were put in separate crucibles in a low vacuum chamber ($\sim 70\ \text{kPa}$; PELCO 2245) along with the undoped spiro-OMeTAD thin films on glass substrates. A Petri dish that contained DMSO was heated at 55°C in the vacuum chamber while the substrate and HBr container remained at the ambient temperature. The exposure time was varied to control the doping concentration in the film. We show the schematic illustration of the set-up for the vapour process doping in Supplementary Fig. 2.

Preparation of MeO–TPD thin films doped with the DMSO–HBr adduct in a solution process. DMSO (150 μl) was added into 500 μl of aqueous HBr (48 wt%) and the solution was mixed by a vortex mixer for 1 min. The DMSO–HBr solution (10 μl), the adduct-forming agent, was added to 2.5 ml of a MeO–TPD (0.32 mM) solution in chlorobenzene. The solution was mixed by a vortex mixer for 1 min and then kept for 20 min at room temperature to prepare a heavily doped MeO–TPD solution. The heavily doped MeO–TPD solution (50 μl) was added to 150 μl of undoped MeO–TPD solution (80 mM) in chlorobenzene and the solution was kept for at least 10 min before the thin-film preparation. The doped MeO–TPD solution was spin coated onto the substrate at 2,500 r.p.m. for 45 s (acceleration, 500 r.p.m.).

Preparation of a spiro-OMeTAD thin film doped with (\pm)-10-CSA, DMSO and HBr. CSA (30 mg) ((\pm)-10-CSA, 98%; Aldrich) was dissolved in 10 μl of DMSO and 300 μl of chlorobenzene. The solution was vortexed until the CSA dissolved completely. Aqueous HBr (3 μl , 48 wt%) was added to the CSA solution and the solution was vortexed for 30 s. DMSO–HBr–CSA solution (50 μl) was added into 500 μl of spiro-OMeTAD solution (7.78 mM) in chlorobenzene to form a heavily doped spiro-OMeTAD solution. The heavily doped spiro-OMeTAD solution (5–50 μl) was added to the undoped spiro-OMeTAD chlorobenzene solution (70 mM) and kept for 15 min before the preparation of the thin films. The spiro-OMeTAD solution was spin coated onto the perovskite layer at 2,500 r.p.m. for 45 s (acceleration, 500 r.p.m.). The molar ratio of DMSO, HBr and CSA was $\sim 1:0.09:1$.

Preparation of a MeO–TPD thin film doped with DMSO–HBr–CSA. CSA (30 mg) was dissolved in 10 μl of DMSO and 300 μl of chlorobenzene. The solution was vortexed until the CSA dissolved completely. Aqueous HBr (3 μl , 48 wt%) was added to the CSA solution and the solution was vortexed for a further 30 s. DMSO–HBr–CSA solution (50 μl) was added into 500 μl of MeO–TPD solution (6.87 mM) in chlorobenzene to prepare a heavily doped MeO–TPD solution. The heavily doped MeO–TPD solution (5 μl) was added to 105 μl of the undoped MeO–TPD chlorobenzene solution (80 mM) and kept for 10 min before the preparation of the thin films. The MeO–TPD solution was spin coated onto the substrate at 2,500 r.p.m. for 45 s (acceleration, 500 r.p.m.).

Asymmetric doping with DMSO–HBr–CSA. Preparation of substrate. FTO-coated glass sheets (TEC7, $7\ \Omega\ \text{sq}^{-1}$; Pilkington) were etched with zinc powder and 2 M HCl to obtain the required electrode pattern. The sheets were then washed with a 2% Hellmanex solution in water followed by sonication for 10 min and then washed with deionized water, acetone, ethanol and isopropanol. The last traces of organic residues were removed by oxygen plasma cleaning for 10 min.

Preparation of the stock solution of DMSO–HBr–CSA. CSA (30 mg) was dissolved in a solution of 20 μl of DMSO, 10 μl of aqueous HBr (48 wt%), 250 μl of acetonitrile (anhydrous, 99.8%; Aldrich) and 50 μl of 2-ethoxyethanol (99%; Aldrich). The molar ratio of DMSO, HBr and CSA was always kept at $\sim 2:0.3:1$. The DMSO–HBr–CSA stock solution was diluted in an acetonitrile and 2-ethoxyethanol mixture (5:1 volume ratio) to change the concentration of CSA.

Preparation of hole-only device with the doping at the HTM/Au interface. Poly-TPD solution (50 mg in 1 ml of toluene) was spin coated onto the FTO substrate at 2,000 r.p.m. for 45 s (acceleration, 500 r.p.m.) and the film was annealed on a hotplate at 100°C for 5 min. The DMSO–HBr–CSA stock solution (concentration of CSA was $\sim 0.25\text{--}25\ \text{mM}$) was spin coated onto the undoped poly-TPD layer at 4,000 r.p.m. for 45 s (acceleration, 500 r.p.m.). The treated thin film was annealed on a hotplate at 100°C for 5 min. Note that this annealing process is enough for the unreacted chemicals, by-products and unstable dopant counterions to leave the organic semiconductor matrix. To control the concentration of dopant on the poly-TPD surface, the stock solution of DMSO–HBr–CSA solution was diluted in acetonitrile and 2-ethoxyethanol (5:1 volume ratio) before the spin coating on the undoped poly-TPD layer. The top Au layer was prepared by the thermal evaporation of Au in vacuum (5×10^{-6} torr).

Preparation of hole-only device with the doping at the FTO/HTM interface. The DMSO–HBr–CSA stock solution (concentration of CSA was $\sim 0.5\text{--}50\ \text{mM}$) was spin coated onto a precleaned FTO substrate. Poly-TPD solution (50 mg in 1 ml of toluene) was spin coated onto the DMSO–HBr–CSA-coated FTO substrate at 2,000 r.p.m. for 45 s (acceleration, 500 r.p.m.) and the film was annealed on the hotplate at 100°C for 5 min. To control the concentration of the dopant at the FTO–poly-TPD film interface, the DMSO–HBr–CSA stock solution was diluted in acetonitrile and 2-ethoxyethanol (5:1 volume ratio), prior to the spin coating.

Preparation of hole-only device with uniform doping at the HTM. The CSA–DMSO–HBr stock solution (50 μl , 40 mM) was added into 1 ml of poly-TPD solution (50 mg ml^{-1}). Poly-TPD was deposited on the FTO substrate at 2,000 r.p.m. for 45 s (acceleration, 500 r.p.m.) and the film was annealed on the hotplate at 100°C for 10 min.

Fabrication of organic transistors. The DMSO–HBr adduct-forming agent (4 μl) was added to 1 ml of C_{16} IDT–BT solution (0.05 mg ml^{-1} in chlorobenzene). The C_{16} IDT–BT/DMSO–HBr solution was again mixed by a vortex mixer for 1 min and then kept for 20 min at room temperature as the doped C_{16} IDT–BT stock solution. Moderately doped (30 μl) and heavily doped (50 μl) C_{16} IDT–BT stock solution was added to 150 μl of the pristine C_{16} IDT–BT solution (13.33 mg ml^{-1} in chlorobenzene). Finally, to obtain a final solution concentration of 10 mg ml^{-1} to prepare C_{16} IDT–BT OTFTs, the pristine C_{16} IDT–BT solution (0.05 mg ml^{-1} in chlorobenzene) was added into both the as-prepared moderately doped and heavily doped C_{16} IDT–BT solutions. The solutions were kept for >10 min before the thin-film deposition.

OTFTs were fabricated in a top-gate bottom-contact architecture on $2.54 \times 2.54\ \text{cm}^2$ glass substrates. The source and drain electrodes of Al/Au (5/35 nm) and Al (40 nm) for the p-type and n-type, respectively, devices were thermally deposited through metal shadow masks on the glass substrates. The channel width and length employed were 1,000 μm and 30 μm , respectively. The pristine and doped C_{16} IDT–BT films (10 mg ml^{-1}) were deposited using spin coating at 2,000 r.p.m. for 60 s, followed by a thermal annealing step at 70°C for 10 min. A 900-nm-thick CYTOP film was deposited on top of the C_{16} IDT–BT films by spin coating at 2,000 r.p.m. for 60 s followed by annealing at 50°C for 2 h. The entire thin-film deposition process was carried out in a nitrogen atmosphere. The geometrical capacitance of the CYTOP layers was measured to be $\sim 2.1\ \text{nF cm}^{-2}$. Finally, a 40-nm-thick Al layer was thermally evaporated through metal shadow masks as the gate electrode to complete the OTFT structures.

Preparation of the doped spiro-OMeTAD film with an adduct dopant for PSCs. The DMSO–HBr adduct-forming agent solution (10 μl) was added to 2.5 ml of a spiro-OMeTAD (0.28 mM) solution in chlorobenzene (anhydrous, $\geq 99.9\%$; Aldrich). The solution was mixed by a vortex mixer for 1 min and then kept for 20 min at room temperature to prepare a heavily doped spiro-OMeTAD solution. The heavily doped spiro-OMeTAD solution (3 μl) was added to 1 ml of undoped spiro-OMeTAD solution (70 mM) in chlorobenzene and the solution was incubated at room temperature for at least 10 min. *tert*-butylpyridine (30 μl) and 20 μl of LiTFSI in acetonitrile (520 mg ml^{-1}) were added to 1 ml of the above-mentioned doped spiro-OMeTAD solution. The resulting solution was spin coated onto the perovskite layer at 2,500 r.p.m. for 45 s (acceleration, 500 r.p.m.). Then, 1.5 μl of DMSO and 5 μl of HBr were put in a vacuum chamber ($\sim 70\ \text{kPa}$) along with the predoped spiro-OMeTAD thin film. The Petri dish that contained DMSO was heated at 55°C in the vacuum chamber while the substrate and HBr container remained at the ambient temperature. The exposure time was 20 s for the optimum condition.

Fabrication of PSCs. FTO-coated glass sheets (TEC7, $7\ \Omega\ \text{sq}^{-1}$; Pilkington) were etched with zinc powder and 2 M HCl to obtain the required electrode pattern.

The sheets were washed with a 2% Hellmanex solution in water and then washed with deionized water, acetone, ethanol and isopropanol. The last traces of organic residues were removed by oxygen plasma cleaning for 10 min. SnO_2 compact layers were then fabricated on the cleaned FTO substrates via spin coating and chemical bath deposition from an SnO_2 precursor solution⁴⁶. To obtain the $\text{FA}_{0.83}\text{Cs}_{0.17}\text{Pb}(\text{I}_{0.85}\text{Br}_{0.15})_3$ precursor solutions, FA iodide, CsI, PbBr_2 and PbI_2 were dissolved in a mixed solvent of anhydrous N,N -dimethylformamide (Aldrich) and anhydrous DMSO (Aldrich) in a 4:1 volume ratio to obtain a stoichiometric solution with the desired composition and a molar concentration of 1.4 M. The perovskite precursor solution was coated onto the SnO_2 substrate by a consecutive two-step spin-coating process, step one at 1,000 r.p.m. for 10 s and step two at 5,000 r.p.m. for 25 s under a low humidity (15–20% at 20 °C) condition with a dry compressed air purge in a dry box. Anisole and chlorobenzene (200 μL) in a 9:1 volume ratio was dropped onto the precrystallized perovskite film for first 8–10 s during the second step of the spin coating. The perovskite films were annealed at 80 °C for 5 min and then at 100 °C for 60 min in a box oven in ambient humidity conditions. Spiro-OMeTAD thin films were deposited on the perovskite films as described in above. Au contact layers (80 nm thick) were deposited as the counter electrodes on the HTM layers by thermal evaporation.

For PTAA-based devices, a PTAA toluene solution (10 mg mL^{-1}) was prepared. To fabricate the undoped device, PTAA was spin coated onto the perovskite layer at 4000 rpm for 45 sec (acceleration: 500 rpm) and the sample was annealed on a hot plate at 100 °C for 5 minutes. To fabricate doped device, 30 mg of CSA (Aldrich, (\pm)-10-CSA, 98%) was dissolved in 10 μL of DMSO and 300 μL of chlorobenzene. The solution was vortexed until CSA was dissolved completely. 3 μL of HBr (48 wt% in water) was added to the CSA solution and the solution was vortexed for 30 seconds. 1 μL of CSA solution was added to the un-doped PTAA solution and was kept for 15 min before the preparation of thin films. PTAA spin coated onto the perovskite layer at 4000 rpm for 45 sec (acceleration: 500 rpm) and the sample was annealed on the hot plate at 100 °C for 5 min.

Fabrication of OLEDs with doped and undoped MeO-TPD as HTM. ITO-coated glass sheets (15 Ω per sheet) were sonicated with 2% Hellmanex in water for 10 min and then washed with deionized water, acetone, ethanol and isopropanol followed by oxygen plasma cleaning for 10 min. MeO-TPD (50 mg) in chlorobenzene was stirred at 80 °C for 30 min. The MeO-TPD solutions (undoped or doped with DMSO–HBr or DMSO–HBr–CSA) were spin coated onto the ITO substrates at 2,500 r.p.m. for 45 s (acceleration, 500 r.p.m.). The substrate was then transferred to a vacuum chamber (CreaPhys GmbH), where Alq_3 , BPhen (both from Luminescence Technologies) and Al (Kurk J. Lesker) were thermally sublimed at rates of 0.4 \AA s^{-1} , 0.4 \AA s^{-1} and 1.5 \AA s^{-1} , respectively, at a base pressure of $<10^{-6}$ mbar. During deposition, the substrates were held at room temperature. The thickness of each layer was 100, 8 and 100 nm, respectively. For p-doping with F4TCNQ, 4 mol% of F4TCNQ was added to the MeO-TPD solution in chlorobenzene and the spinning condition for the MeO-TPD layer was the same as that for the other undoped devices⁴⁷.

Reporting summary. Further information on research design is available in the Nature Research Reporting Summary linked to this article.

Data availability

The datasets used in this work are available in the Oxford University Research Archive repository⁴⁸.

References

- Anaraki, E. H. et al. Highly efficient and stable planar perovskite solar cells by solution-processed tin oxide. *Energy Environ. Sci.* **9**, 3128–3134 (2016).
- Huang, Q. et al. Highly efficient top emitting organic light-emitting diodes with organic outcoupling enhancement layers. *Appl. Phys. Lett.* **88**, 113515 (2006).

- Sakai, N. et al. *Adduct-Based p-Doping of Organic Semiconductors* (Oxford University Research Archive, 2021); <https://doi.org/10.5287/bodleian:zrMDxRzzB>

Acknowledgements

This research has mainly received funding from the European Commission (PERTPV-agreement no. 763977) and EPSRC (EP/M005143/1 and EP/S004947/1). M.R. has received funding from the EC FP 7 MSCA—Career Integration Grant (630864) and M.R. and S.V.K. acknowledge funding from the EPSRC WAFT project (EP/M015173/1). R.W. is supported by EPSRC CDT Plastic Electronics (EP/L016702/1). P.K.N. acknowledges support from the Department of Atomic Energy, Government of India, under Project Identification no. RTI 4007 and SERB India core research grant (CRG/2020/003877). F.Z., X.L. and A.K. acknowledge funding from National Science Foundation under grants DMR-1506097 and DMR-1807797. S.N. acknowledges Marie Skłodowska-Curie Actions individual fellowships (grant agreement no. 659306) and a start-up grant from CSIR-IMMT, India. T.M. and V.G. acknowledge funding from European Regional Development Fund (project no. 01.2.2-LMT-K-718-03-0040) under a grant agreement with the Research Council of Lithuania (LMTLT). T.D.A. and A.B. are grateful to King Abdullah University of Science and Technology (KAUST), KAUST Solar Centre and KAUST Office for Sponsored Research (OSR) for the financial support under award no: OSR-2019-CRG8-4095, no. OSR-2018-CARF/CCF-3079. J.L. and C.G. are grateful for support for the NanoSIMS facility from EPSRC under grant EP/M018237/1. We thank I. McPherson for his help in mass spectrometry measurements and M. Heeney for providing the C16IDT-BT polymer.

Author contributions

N.S. and P.K.N. conceived and executed the initial proof-of-concept experiments and unravelled the mechanism of doping. P.K.N. proposed the dopant system. H.J.S. proposed the asymmetric doping and N.S. designed and performed the experiments. N.S. and R.W. performed the conductivity measurements. N.S. and R.W. performed the doping stability test under the supervision of M.R. S.V.K. performed the ellipsometry measurements, analyses and simulation under the supervision of M.R. R.W. fabricated the OLEDs under the supervision of M.R. and N.S. fabricated all the other devices used in this work. S.N. and P.K.N. performed the attenuated total reflection FTIR measurements. F.Z. and X.L. did the UPS, XPS and Kelvin probe measurements under the supervision of A.K. F.Z. did the AFM measurements. J.L. did the nanosecond ion mass spectrometry measurements with inputs from P.K.N. and N.S. C.G. planned and helped interpret the nanosecond ion mass spectrometry measurements. N.S. and Y.-H.L. performed the capacitance–voltage measurements. H.S.B. performed the quantum chemical calculations. T.M. conducted the synthesis of the HTM V886 and V.G. supervised the synthesis. A.B. fabricated the OTFTs and performed the electrical characterization under the supervision of T.D.A. T.D.A., Y.-H.L. and A.B. interpreted the results and provided the analysis of the OTFTs. N.S. and P.K.N. wrote the first draft. All the authors contributed to the analysis of the results, discussion of the content and revisions of the manuscript. P.K.N. and H.J.S. supervised the project.

Competing interests

A patent based on this work has been filed (international application number PCT/GB2018/053014) by the University of Oxford. H.J.S. is a co-founder of Oxford PV Ltd and Helio Display Materials. The remaining authors declare no competing interests.

Additional information

Supplementary information The online version contains supplementary material available at <https://doi.org/10.1038/s41563-021-00980-x>.

Correspondence and requests for materials should be addressed to P.K.N. or H.J.S.

Peer review information *Nature Materials* thanks Adam Moule and the other, anonymous, reviewer(s) for their contribution to the peer review of this work.

Reprints and permissions information is available at www.nature.com/reprints.

Solar Cells Reporting Summary

Nature Research wishes to improve the reproducibility of the work that we publish. This form is intended for publication with all accepted papers reporting the characterization of photovoltaic devices and provides structure for consistency and transparency in reporting. Some list items might not apply to an individual manuscript, but all fields must be completed for clarity.

For further information on Nature Research policies, including our [data availability policy](#), see [Authors & Referees](#).

► Experimental design

Please check: are the following details reported in the manuscript?

1. Dimensions

- | | | |
|--|--|--|
| Area of the tested solar cells | <input checked="" type="checkbox"/> Yes
<input type="checkbox"/> No | The active area of the solar cell was 0.0919 cm ² . |
| Method used to determine the device area | <input checked="" type="checkbox"/> Yes
<input type="checkbox"/> No | We used an opaque metal mask (aperture area is 0.0919 cm ²) to define the active area and to eliminate edge effects. The electronic active area (i.e. the overlap of the FTO electrode and metal electrode) of the cell was ~ 0.12 cm ² . |

2. Current-voltage characterization

- | | | |
|--|--|---|
| Current density-voltage (J-V) plots in both forward and backward direction | <input checked="" type="checkbox"/> Yes
<input type="checkbox"/> No | We show the J-V from scans in both forward and backward directions in Supplementary Figure 38-39, and Supplementary Table 6. |
| Voltage scan conditions
<i>For instance: scan direction, speed, dwell times</i> | <input checked="" type="checkbox"/> Yes
<input type="checkbox"/> No | Current-voltage measurements were typically scanned from +1.4 V to 0 V and 0 V to +1.4 V. The step voltage was fixed at 30 mV, a delay time between scans at each voltage step was set to 0.01 s. |
| Test environment
<i>For instance: characterization temperature, in air or in glove box</i> | <input checked="" type="checkbox"/> Yes
<input type="checkbox"/> No | In atmospheric air at room temperature (20 - 30 degree celsius). |
| Protocol for preconditioning of the device before its characterization | <input checked="" type="checkbox"/> Yes
<input type="checkbox"/> No | Typically, a stabilization time of 5 s at forward bias of 1.4 V under illumination was done prior to scanning. For the devices in Figure 5 were stabilized at forward bias of 1.2 V for 5 s. |
| Stability of the J-V characteristic
<i>Verified with time evolution of the maximum power point or with the photocurrent at maximum power point; see ref. 7 for details.</i> | <input checked="" type="checkbox"/> Yes
<input type="checkbox"/> No | We show stabilized power output (SPO) data, determined by holding the cell at a fixed voltage near the maximum power point (MPP) on the J-V curve for 60 s. |

3. Hysteresis or any other unusual behaviour

- | | | |
|---|--|---|
| Description of the unusual behaviour observed during the characterization | <input checked="" type="checkbox"/> Yes
<input type="checkbox"/> No | We show the J-V from scans in both forward and backward directions in Supplementary Figure 38 and 39. We also discuss the stabilized power output in the text where we present the device performance (Figure 5). |
| Related experimental data | <input checked="" type="checkbox"/> Yes
<input type="checkbox"/> No | We show the J-V from scans in both forward and backward in Supplementary Figure 38 and 39. |

4. Efficiency

- | | | |
|---|--|--|
| External quantum efficiency (EQE) or incident photons to current efficiency (IPCE) | <input checked="" type="checkbox"/> Yes
<input type="checkbox"/> No | We provided the EQE data under the standard reference spectrum which is comparable with the simulator. The EQE spectra were evaluated via custom-build Fourier transform photocurrent spectroscopy based on the Bruker Vertex 80v Fourier transform spectrometer. A Newport AAA sun simulator was used as light source and the light intensity was calibrated with a Newport-calibrated reference silicon photodiode. We show the EQE data in Supplementary Figure 37. |
| A comparison between the integrated response under the standard reference spectrum and the response measure under the simulator | <input checked="" type="checkbox"/> Yes
<input type="checkbox"/> No | The difference between the integrated current from EQE of typical device (Supplementary Figure 37) and the averaged short-circuit current from the JV curve measured under AM 1.5G solar simulator (Supplementary Table 6) is within 5 %, which is within the accuracy confidence of the measurements. |
| For tandem solar cells, the bias illumination and bias voltage used for each subcell | <input type="checkbox"/> Yes
<input type="checkbox"/> No | <div style="border: 1px solid #ccc; padding: 2px; margin-bottom: 2px;">State where this information can be found in the text.</div> <div style="border: 1px solid #ccc; padding: 2px;">Explain why this information is not reported/not relevant.</div> |

5. Calibration

Light source and reference cell or sensor used for the characterization

☒ Yes
☐ No

The simulated solar light (AAB ABET technologies Sun 2000 solar simulator) with its light intensity, 100 mW cm⁻² (AM 1.5) was calibrated against a standard amorphous-silicon PV cell (NREL-calibrated KG5 filtered silicon reference cell).

Confirmation that the reference cell was calibrated and certified

☒ Yes
☐ No

The intensity was calibrated with an NREL calibrated KG5 filtered Si reference cell. The mismatch factor was estimated to be $M=1.035405$ and the lamp intensity was adjusted to account for this mismatch.

Calculation of spectral mismatch between the reference cell and the devices under test

☒ Yes
☐ No

Fully described in the Supplementary Information

6. Mask/aperture

Size of the mask/aperture used during testing

☒ Yes
☐ No

We used an opaque metal mask (aperture area is 0.0919 cm²) to define the active area and to eliminate edge effects. The electronic active area (i.e. the overlap of the FTO electrode and metal electrode) of the cell was ~ 0.12 cm².

Variation of the measured short-circuit current density with the mask/aperture area

☒ Yes
☐ No

We showed the variation of J_{sc} of each devices in SupplementaryTable 5, which are represented as an average value and the standard deviation ($n>20$).

7. Performance certification

Identity of the independent certification laboratory that confirmed the photovoltaic performance

☐ Yes
☒ No

Explain why this information is not reported/not relevant.

A copy of any certificate(s)

Provide in Supplementary Information

☐ Yes
☒ No

Explain why this information is not reported/not relevant.

8. Statistics

Number of solar cells tested

☒ Yes
☐ No

We showed the variation of solar cell performances of each devices in Supplementary Table 5, which are represented as an average value and the standard deviation ($n>20$).

Statistical analysis of the device performance

☒ Yes
☐ No

We give statistical characteristics of the device performance in Supplementary Figure 35 and SupplementaryTable 5.

9. Long-term stability analysis

Type of analysis, bias conditions and environmental conditions

For instance: illumination type, temperature, atmosphere humidity, encapsulation method, preconditioning temperature

☐ Yes
☒ No

Explain why this information is not reported/not relevant.